(Preprint) AAS 13-307

MARS SCIENCE LABORATORY ENTRY, DESCENT, AND LANDING TRAJECTORY AND ATMOSPHERE RECONSTRUCTION

Christopher D. Karlgaard*, Prasad Kutty†, Mark Schoenenberger‡, Jeremy Shidner§

On August 5th 2012, The Mars Science Laboratory entry vehicle successfully entered Mars' atmosphere and landed the Curiosity rover on its surface. A Kalman filter approach has been implemented to reconstruct the entry, descent, and landing trajectory based on all available data. The data sources considered in the Kalman filtering approach include the inertial measurement unit accelerations and angular rates, the terrain descent sensor, the measured landing site, orbit determination solutions for the initial conditions, and a new set of instrumentation for planetary entry reconstruction consisting of forebody pressure sensors, known as the Mars Entry Atmospheric Data System. These pressure measurements are unique for planetary entry, descent, and landing reconstruction as they enable a reconstruction of the freestream atmospheric conditions without any prior assumptions being made on the vehicle aerodynamics. Moreover, the processing of these pressure measurements in the Kalman filter approach enables the identification of atmospheric winds, which has not been accomplished in past planetary entry reconstructions. This separation of atmosphere and aerodynamics allows for aerodynamic model reconciliation and uncertainty quantification, which directly impacts future missions. This paper describes the mathematical formulation of the Kalman filtering approach, a summary of data sources and preprocessing activities, and results of the reconstruction.

INTRODUCTION

On August 5th 2012, the Mars Science Laboratory (MSL) entry vehicle (EV) successfully entered the Mars atmosphere and landed the Curiosity rover safely on the surface of the planet in Gale crater. MSL carried with it a unique instrumentation package designed to measure the aerodynamic and aerothermal environments during atmospheric entry. This instrumentation package is known as the MSL Entry, Descent, and Landing Instrumentation (MEDLI),[1] which consists of two major subsystems, the Mars Entry Atmospheric Data System (MEADS) and the MEDLI Integrated Sensor Plugs (MISP). The MEADS consists of seven pressure transducers connected to flush orifices in the heat shield forebody to measure the pressure distribution. The MISP devices are a system of thermocouple and recession sensors that provide aerothermal measurements of the heat shield performance. The MEDLI sensors provide key measurements that can be used for trajectory reconstruction and engineering validation of aerodynamic, atmospheric, and thermal protection system models in addition to Earth-based systems testing procedures. Such validation directly benefits future planetary entry, descent, and landing (EDL) by reducing uncertainties associated with these models and procedures.

The basic MEADS science objectives are to reconstruct atmospheric data variables from pressure measurements alone when the free stream dynamic pressure is above 850 Pa. In particular, the objectives are to estimate the angles of attack and sideslip to within 0.5 deg and the dynamic pressure to within 2%, in a 3σ sense. Secondary objectives are to estimate the Mach number, freestream density and atmospheric winds from the MEADS pressure measurements, when combined with the on-board Inertial Measurement Unit (IMU) data. These measurements serve to enhance the MSL trajectory reconstruction and performance analysis, and enable a separation of the aerodynamics from the atmosphere, which prior to MEADS has not been achievable for Mars EDL reconstruction. The concept is an implementation of the Flush Air Data System (FADS). The FADS concept was conceived and developed specifically to provide research quality air data during the hypersonic flight regime where the classical Pitot static probe could not survive.

The MEDLI/MEADS project installed seven pressure ports through the MSL PICA heat shield at strategic locations to acquire heat shield surface pressure data during the atmospheric entry phase at Mars. The

*Supervising Engineer, Analytical Mechanics Associates, Inc., Hampton VA. Senior Member AIAA, Member AAS.
†Project Engineer, Analytical Mechanics Associates, Inc., Hampton VA.
‡Aerospace Engineer, Atmospheric Flight and Entry Systems Branch, NASA Langley Research Center, Hampton, VA. Senior Member AIAA.
§Senior Project Engineer, Analytical Mechanics Associates, Inc., Hampton, VA. Senior Member AIAA.

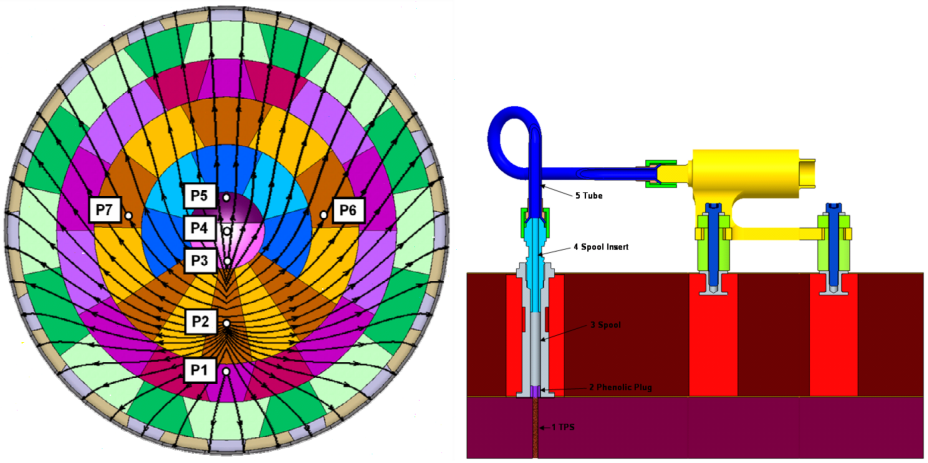

(a) MEDLI/MEADS Pressure Port Locations (b) MEDLI/MEADS Tube Configuration

Figure 1. MEDLI/MEADS Geometry

MEADS pressure ports are located on the MSL heat shield as shown in Figure 1(a). The PICA tile layout is also shown in this figure along with the predicted flow streamlines over the surface of the Thermal Protection System (TPS). All of the pressure ports are located a minimum of 3-inches from the PICA tile seams. At each of the pressure port locations there is an independent pressure measurement system installed on the internal surface of the heat shield support structure.

Pressure ports P1 and P2 are located in the stagnation region to provide a nearly direct measurement of the total pressure in the high Mach regime. Ports P3, P4, and P5 lie on the spherical cap and are placed in order to take advantage of the simple geometry for angle-of-attack measurements. Additionally, P4, located at the geometric center, provides a nearly direct total pressure measurement at the low Mach regime prior to parachute deployment. The final two ports are located in the horizontal plane of symmetry, approximately 1.0 meters off of the centerline. The ports P6 and P7 provide the off-axis measurements needed to estimate the angle of sideslip. The pressure ports are connected to pressure transducers via a tube system illustrated in Figure 1(b). The measured pressures are sampled at a rate of 8 Hz during entry.

The MEADS trajectory reconstruction approach relies on four separate reconstruction methods. The first three of these techniques are semi-independent methods that utilize different portions of the entire data set. These techniques include a pure inertial reconstruction, an aerodatabase reconstruction, and a MEADS pressure reconstruction. The fourth reconstruction is a combined approach in which all available data are processed together using a Kalman filter technique.

The pure inertial reconstruction is based on a direct numerical integration of the measured accelerations and angular rates, using initial conditions obtained from orbit determination. An assumed atmosphere profile based on mesoscale models can be utilized to produce atmospheric-relative quantities such as Mach number and dynamic pressure.

The aerodatabase reconstruction uses the sensed accelerations and the assumed vehicle aerodynamic database to produce estimates of the freestream atmospheric profile and the angles of attack and sideslip. The method first estimates density from the axial acceleration and axial force coefficient, and then ratios of normal to axial force coefficients and side to axial force coefficients to produce estimates of angle of attack and sideslip, respectively.

The first two of the semi-independent reconstructions have long been used for planetary entry, descent, and landing reconstructions. The third method, using the MEADS pressures, is new for this application. The MEADS pressure reconstruction utilizes a nonlinear least-squares algorithm to produce estimates of angle of attack, angle of sideslip, dynamic pressure, and static pressure. The least-squares algorithm includes a novel IMU-aiding approach in which the IMU velocity is used to improve the estimate of Mach number. Atmospheric density is computed from the dynamic pressure estimate and the IMU velocity, assuming no winds. The MEADS dynamic pressure and IMU acceleration and angular rate measurements can also be combined to produce estimates of the vehicle aerodynamic forces and moments.

Results from these semi-independent reconstructions are documented in Ref. 2. The overall good data quality and general agreement between the three reconstructions supports a combined reconstruction involving Kalman filtering techniques to optimally blend all available data together into a single trajectory and

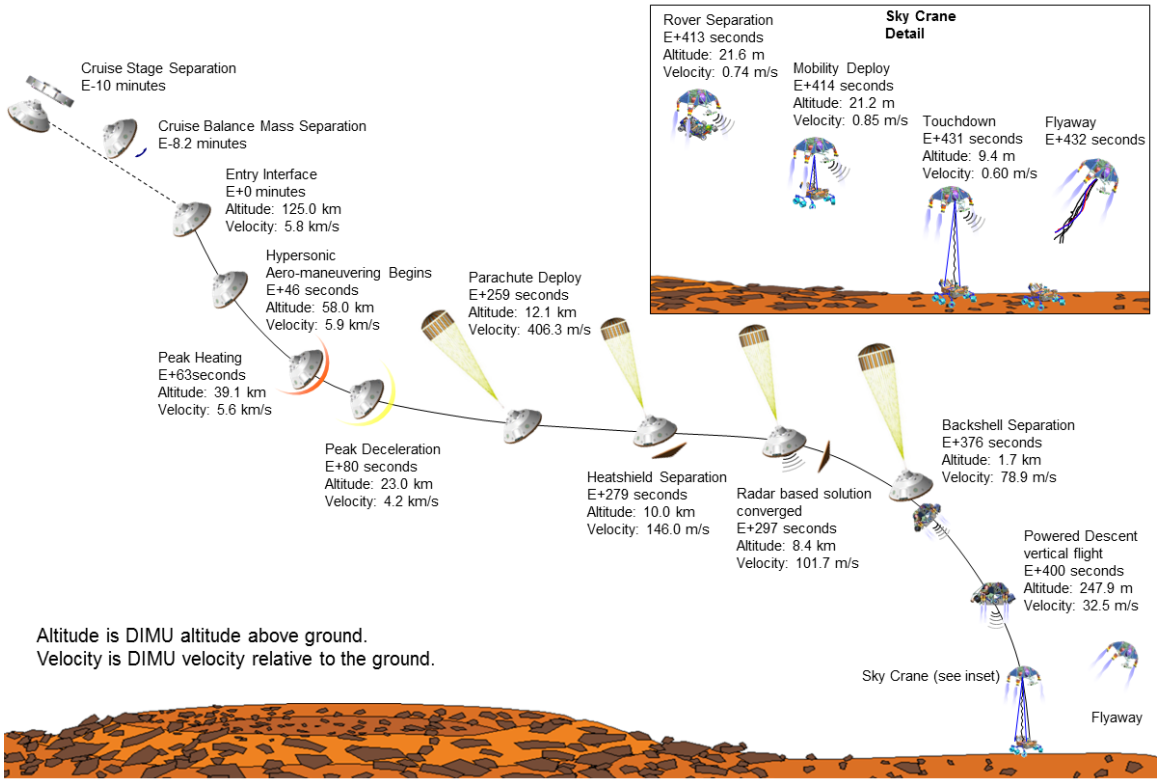

Figure 2. MSL Entry, Descent, and Landing

atmosphere estimate, which is the topic of this paper.

This paper provides an overview of the Kalman filter approach for MSL/MEADS trajectory reconstruction and the results of the reconstruction. An overview of the raw data is provided, along with an assessment of data quality. Techniques used to preprocess the data are described, which includes editing out suspect data and smoothing to reduce noise. The MISP sensors and associated modeling and reconstruction techniques are documented in Ref. 3 and are not discussed further in this paper.

MARS SCIENCE LABORATORY ENTRY, DESCENT, AND LANDING OVERVIEW

Figure 2 shows a timeline of the different EDL events.[4] EDL consists of six major segments: Exo-Atmospheric, Entry, Parachute Descent, Powered Descent, Sky Crane, and Fly Away.[5] The Exo-Atmospheric segment begins once the cruise stage separation command is sent. Once the cruise stage separates, Guidance, Navigation, and Control (GNC) is enabled. Once enabled, the entry body is despun and turned to its entry attitude. Then, the two 75-kg Cruise Balance Masses (CBMs) are jettisoned to enable aerodynamic lift.

The Entry segment starts with the vehicle at the Entry Interface Point (EIP) defined at 3522.2 km from the center of Mars, approximately 540 seconds after cruise stage separation. During the Entry segment, the vehicle goes through peak heating and peak deceleration, the Reaction Control System (RCS) controls the lift vector to achieve the desired down-range and cross-range target. Just prior to parachute deployment, six 25-kg Entry Balance Masses (EBMs) are jettisoned to eliminate lift and the vehicle rolls to point the Terminal Descent Sensor (TDS) to the ground. This maneuver is called the Straighten Up and Fly Right (SUFR) maneuver.

The Parachute descent segment starts with the parachute deployment triggered once the vehicle reached Mach 1.7. Once the vehicle achieves a speed of Mach 0.7, the heat shield is jettisoned and the TDS starts acquiring the ground. Note that the MEDLI instruments are powered off 10 seconds prior to heat shield jettison. The command to jettison the backshell and the parachute is issued at an altitude of 1.6 km and at a velocity of approximately 79 m/s. Just before backshell separation, the Mars Landing Engines (MLEs) are primed in preparation for the start of the powered descent segment.

The Powered Descent segment begins at backshell separation. During powered descent, eight independently throttleable MLEs are actuated, initially to execute a divert maneuver for backshell avoidance which brings the vehicle to vertical flight at a descent rate of 32 m/s. Once vertical flight is achieved, a descent at constant velocity to adjust for altitude error at backshell separation starts. This constant velocity phase is

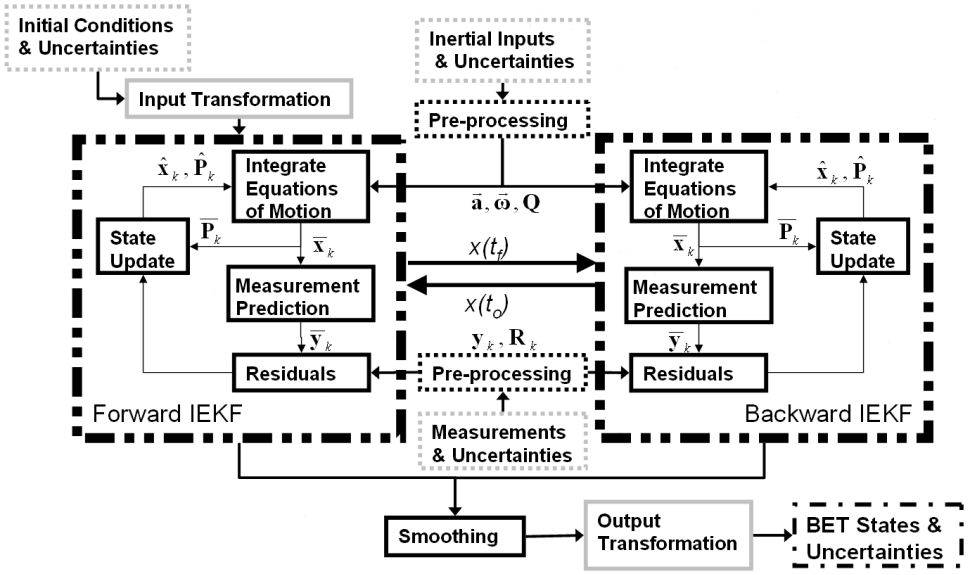

Figure 3. NewSTEP Flow Diagram

followed by a constant deceleration phase, which reducs the vehicle's speed to 0.75 m/s in preparation for the sky crane segment. At this time, the four inboard MLEs are throttled down to near shutdown (1%) while the four remaining MLEs were throttled at 50%.

The Sky Crane segment starts following issuance of the rover separation command, which occurrs at an altitude of approximately 18.6 m. The rover is lowered to 7.5 m below the descent stage. Then, the descent stage continues to descend until post-touchdown is detected.

The Fly Away segment starts after touchdown is sensed. Once the descent stage stops its vertical motion, the bridle and electrical umbilical devices are cut and two of the MLE engines are throttled up to 100% while the other two engines are at slightly less than 100%. This causes the descent stage to pitch to 45 degrees. Once the turn maneuver is completed, all four engines are throttled up to 100%. Constant thrust is applied to ensure the descent stage impacts the surface at least 300 m from the landing point.

TRAJECTORY AND ATMOSPHERE RECONSTRUCTION APPROACH

Overview

The Kalman filter based trajectory reconstruction is calculated using a statistical trajectory estimation program known as NewSTEP. This trajectory estimation program is a Matlab-based Iterative Extended Kalman Filter (IEKF) code that computes optimal 6-DOF trajectory estimates based on all available measurement data along with uncertainty estimates. This code is a generalization of the Statistical Trajectory Estimation Program (STEP)[7] developed by NASA/LaRC and used extensively in the 1960s-1980s on a wide variety of launch vehicle and entry vehicle flight projects. The NewSTEP code borrows heavily from the STEP formulation, but includes several enhancements to the algorithms and implementation, such as the addition of the iterative Kalman filter capability and new measurement types.

A flowchart illustrating the reconstruction data processing scheme implemented in NewSTEP is shown in Fig. 3. The inputs to the reconstruction method consist of initial conditions, inertial measurement data in the form of linear accelerations and angular rates, and various observed quantities such as radar and air data measurements. Additionally, uncertainties on all these input data sources must be provided for the proper weighting to be assigned to the data in the filtering algorithm. It is important that the input uncertainties be realistic in order to avoid improper weighting: measurement data with uncertainties set erroneously low can introduce non-physical dynamics because the filter will essentially track the noise. These inputs are shown with the dashed gray boxes in Fig. 3. Pre-processing is conducted to perform any coordinate transformations that may be necessary, and to improve data quality by reducing noise, eliminating systematic errors, and editing potentially bad data that sometimes can arise. Note that the data pre-processing should be done carefully to avoid introducing artificial errors such as smoothing artifacts, and that the input uncertainties can be adjusted to accurately reflect improvements in data quality. The pre-processing and the input transformations are shown with the dashed black and solid gray boxes in Fig. 3, respectively.

The core data processing algorithm consists of a forward and backward IEKF that together, when merged using the Fraser-Potter smoothing algorithm,[12] form optimal state estimates based on all available data. The forward and backward filter algorithms are shown in the black boxes in Fig. 3. The Kalman filter algorithm is reviewed in more detail in the next section, but at a high level it is a predictor/corrector algorithm in which state predictions are computed from numerical integration of the rigid body equations of motion, and corrections to the estimate are computed from a weighted least-squares fit of state to the observed data. The forward filter processes the data in this manner starting from the initial time, propagating through all the observed data. Since the end point of the forward pass has benefited from all available measurement data, but the earlier points in the trajectory have benefited from data recorded only up to that time, a backward pass is implemented that propagates the state estimate back to the initial time point. These two passes are fused using the Fraser-Potter smoothing algorithm, so that each data point in the BET is estimated from all available data.

Lastly, output transformations are conducted to generate estimates of quantities of interest, such as Mach number and dynamic pressure, which are not internal state variables estimated in the Kalman filter. These transformations include uncertainty transformations that map the internal state uncertainties into output uncertainties. The end result of this process is the BET, shown in the black dash-dot box, which includes vehicle trajectory estimates along with uncertainties.

Algorithm

The Kalman filter is a recursive weighted least-squares estimation procedure that optimally blends sensor data and mathematical models to produce minimum variance estimates of the system state. Let the system dynamics be represented by a mixed continuous-discrete nonlinear model of the form

$$\dot{\boldsymbol{x}} = \boldsymbol{f}(\boldsymbol{x}, \boldsymbol{u}, \boldsymbol{\eta}, t) \tag{1}$$

$$\boldsymbol{y} = \boldsymbol{g}(\boldsymbol{x}, \boldsymbol{u}, \boldsymbol{\xi}, t) \tag{2}$$

where $\boldsymbol{x}$ is the filter state with continuous dynamics, $\boldsymbol{u}$ is a deterministic input, $\boldsymbol{\eta}$ is a stochastic input to the equations of motion (process noise), $\boldsymbol{y}$ is the measurement that is available at discrete time intervals, and $\boldsymbol{\xi}$ is the measurement noise.

Let the quantities $\hat{\boldsymbol{x}}_{k-1}$ and $\hat{\boldsymbol{P}}_{k-1}$ be the state estimate and state estimate error covariance matrix at time t_{k-1}, respectively, and let $\bar{\boldsymbol{x}}_k$ and $\bar{\boldsymbol{P}}_k$ be the predicted state and covariance at time t_k, computed from numerical integration of the continuous process dynamics and the linear covariance propagation equation[13]

$$\dot{\boldsymbol{P}} = \boldsymbol{A}(t)\boldsymbol{P}(t) + \boldsymbol{P}(t)\boldsymbol{A}(t)^T + \boldsymbol{B}(t)\boldsymbol{Q}(t)\boldsymbol{B}(t)^T \tag{3}$$

where $\boldsymbol{A}(t)$ is the linearization of the system dynamics with respect to the state, $\boldsymbol{B}(t)$ is the linearization of the system dynamics with respect to the process noise inputs, and $\boldsymbol{Q}(t)$ is the process noise spectral density.

Then, the measurement $\boldsymbol{y}_k$ at time t_k is processed according to[13]

$$\hat{\boldsymbol{x}}_{k,i+1} = \bar{\boldsymbol{x}}_k + \boldsymbol{K}_{k,i}\left[\boldsymbol{y}_k - \boldsymbol{g}(\hat{\boldsymbol{x}}_{k,i}, \boldsymbol{u}_k, \boldsymbol{\xi}_k, t_k) - \boldsymbol{C}_{k,i} \cdot (\bar{\boldsymbol{x}}_k - \hat{\boldsymbol{x}}_{k,i})\right] \tag{4}$$

where i denotes the iteration index and $\boldsymbol{C}$ is the linearization of the measurement model with respect to the state. The quantity $\boldsymbol{K}_{k,i}$ is the Kalman gain matrix, given by[13]

$$\boldsymbol{K}_{k,i} = \bar{\boldsymbol{P}}_k \boldsymbol{C}_{k,i}^T \left[\boldsymbol{C}_{k,i}\bar{\boldsymbol{P}}_k\boldsymbol{C}_{k,i}^T + \boldsymbol{D}_{k,i}\boldsymbol{R}_k\boldsymbol{D}_{k,i}^T\right] \tag{5}$$

where $\boldsymbol{R}_k$ is the measurement noise covariance matrix and $\boldsymbol{D}$ is the linearization of the measurement model with respect to the measurement noise.

The filtering equations listed above are iterated until convergence (or until reaching a prescribed iteration limit), leading to the state estimate that follows from the nonlinear measurement update. The covariance of the state estimate is computed from

$$\hat{\boldsymbol{P}}_k = \left[\boldsymbol{I} - \boldsymbol{K}_k\boldsymbol{C}_k\right]\bar{\boldsymbol{P}}_k\left[\boldsymbol{I} - \boldsymbol{K}_k\boldsymbol{C}_k\right]^T + \boldsymbol{K}_k\boldsymbol{R}_k\boldsymbol{K}_k^T \tag{6}$$

where $\boldsymbol{I}$ is the identity matrix of appropriate dimension.

After processing the IEKF forward and backward through all the available measurement data, the estimates are combined using the Fraser-Potter smoothing algorithm, given by[12]

$$\hat{\boldsymbol{P}}_k = \left[\hat{\boldsymbol{P}}_{f_k}^{-1} + \bar{\boldsymbol{P}}_{b_k}^{-1}\right]^{-1} \tag{7}$$

$$\hat{\boldsymbol{x}}_k = \hat{\boldsymbol{P}}_k\left[\hat{\boldsymbol{P}}_{f_k}^{-1}\hat{\boldsymbol{x}}_{f_k} + \bar{\boldsymbol{P}}_{f_k}^{-1}\bar{\boldsymbol{x}}_{b_k}\right] \tag{8}$$

where $\hat{\boldsymbol{x}}_{f_k}$ and $\hat{\boldsymbol{P}}_{f_k}$ are the forward filtered state and covariance estimates, $\bar{\boldsymbol{x}}_{b_k}$ and $\bar{\boldsymbol{P}}_{b_k}$ are the backward predicted state and covariance estimates, and $\hat{\boldsymbol{x}}_k$ and $\hat{\boldsymbol{P}}_k$ are the smoothed state and covariance estimates.

Equations of Motion

The filter state variables used in this formulation are

$$\boldsymbol{x} = \left[\begin{array}{ccccccccccccccc} r & \theta & \phi & u & v & w & e_0 & e_1 & e_2 & e_3 & u_w & v_w & w_w & p & \rho \end{array} \right]^T \tag{9}$$

where r is the radius of the vehicle from the center of the planet, θ is the longitude, ϕ is the declination, u, v, w are the inertial velocity components in a topocentric frame (defined by the z-axis direction along the radius vector, toward the center of the planet, and the y-axis to the east) e_i are the Euler parameters describing the attitude of the vehicle with respect to the topodetic frame (north-east-down). The quantities u_w, v_w and w_w are the wind components in the topodetic frame, and p and ρ are the atmospheric pressure and density, respectively.

The state dynamics are modeled with the nonlinear system of differential equations given by[8]

$$\dot{r} = -w \tag{10}$$

$$\dot{\phi} = \frac{u}{r} \tag{11}$$

$$\dot{\theta} = \frac{v}{r\cos\phi} - \Omega \tag{12}$$

$$\left\{ \begin{array}{c} \dot{u} \\ \dot{v} \\ \dot{w} \end{array} \right\} = \boldsymbol{G}^T \left\{ \begin{array}{c} a_x \\ a_y \\ a_z \end{array} \right\} + \left\{ \begin{array}{c} \left(uw - v^2\tan\phi\right)/r - \left(3\mu J_2/2r^4\right)\sin\left(2\phi\right) \\ \left(uv\tan\phi + vw\right)/r \\ -\left(u^2+v^2\right)/r + \mu/r^2 - \left(3\mu J_2/2r^4\right)\left(2-3\cos^2\phi\right) \end{array} \right\} \tag{13}$$

$$\left\{ \begin{array}{c} \dot{e}_0 \\ \dot{e}_1 \\ \dot{e}_2 \\ \dot{e}_3 \end{array} \right\} = \frac{1}{2} \left[\begin{array}{ccc} -e_1 & -e_2 & -e_3 \\ e_0 & -e_3 & e_2 \\ e_3 & e_0 & -e_1 \\ -e_2 & e_1 & e_0 \end{array} \right] \left(\left\{ \begin{array}{c} \omega_x \\ \omega_y \\ \omega_z \end{array} \right\} - \frac{1}{r}\boldsymbol{G} \left\{ \begin{array}{c} v \\ -u \\ -v\tan\phi \end{array} \right\} \right) \tag{14}$$

$$\dot{p} = \frac{\mu\rho w}{r^2} \tag{15}$$

$$\dot{\rho} = \frac{\mu\rho^2 w}{r^2 p} \tag{16}$$

$$\dot{u}_w = 0 \tag{17}$$

$$\dot{v}_w = 0 \tag{18}$$

$$\dot{w}_w = 0 \tag{19}$$

where μ is the planetary gravitational parameter, J_2 is the planetary oblateness coefficient, Ω is the angular rate of the planet.

The matrix $\boldsymbol{G}$ is the transformation from the topocentric frame to the body frame, given by $\boldsymbol{G} = \boldsymbol{G}_d\boldsymbol{G}_\phi$, where

$$\boldsymbol{G}_d = \left[\begin{array}{ccc} e_0^2+e_1^2-e_2^2-e_3^2 & 2\left(e_1e_2+e_0e_3\right) & 2\left(e_1e_3-e_0e_2\right) \\ 2\left(e_1e_2-e_0e_3\right) & e_0^2-e_1^2+e_2^2-e_3^2 & 2\left(e_0e_1+e_2e_3\right) \\ 2\left(e_1e_3+e_0e_2\right) & 2\left(e_2e_3-e_0e_1\right) & e_0^2-e_1^2-e_2^2+e_3^2 \end{array} \right] \tag{20}$$

$$\boldsymbol{G}_\phi = \left[\begin{array}{ccc} \cos\left(\phi-\phi_{gd}\right) & 0 & \sin\left(\phi-\phi_{gd}\right) \\ 0 & 1 & 0 \\ -\sin\left(\phi-\phi_{gd}\right) & 0 & \cos\left(\phi-\phi_{gd}\right) \end{array} \right] \tag{21}$$

The body axis sensed accelerations are transformed from the IMU location according to the relations

$$\left\{ \begin{array}{c} a_x \\ a_y \\ a_z \end{array} \right\} = \left\{ \begin{array}{c} \tilde{a}_x \\ \tilde{a}_y \\ \tilde{a}_z \end{array} \right\} - \left[\begin{array}{ccc} -\left(\omega_y^2+\omega_z^2\right) & \left(\omega_x\omega_y-\dot{\omega}_z\right) & \left(\omega_x\omega_z+\dot{\omega}_y\right) \\ \left(\omega_x\omega_y+\dot{\omega}_z\right) & -\left(\omega_x^2+\omega_z^2\right) & \left(\omega_y\omega_z-\dot{\omega}_x\right) \\ \left(\omega_x\omega_z-\dot{\omega}_y\right) & \left(\omega_y\omega_z+\dot{\omega}_x\right) & -\left(\omega_x^2+\omega_y^2\right) \end{array} \right] \left\{ \begin{array}{c} x_m \\ y_m \\ z_m \end{array} \right\} \tag{22}$$

where $\tilde{a}_x$, $\tilde{a}_y$, and $\tilde{a}_z$ are the sensed accelerations at the IMU location, x_m, y_m and z_m are the position of the IMU with respect to the center of mass in the body frame, and ω_x, ω_y and ω_z are the body axis sensed angular velocity components.

Additive process noise terms are included on the acceleration and angular rate measurements to account for sensor errors. Process noise terms are also included on the atmospheric winds, pressure, and density to account for model uncertainties. Thus, the stochastic wind model is a random walk.

An important feature of the Kalman filter approach is that the wind components are treated as state variables, and as such can be estimated based on the various measurement data, without having to deal with the singularities that arise in application of the method proposed in Reference 14.

Output Transformations

Auxiliary calculations are performed in order to transform the internal filter state into desired output quantities. For example, the angle of attack is not an internal filter state but it is a desired output from the trajectory reconstruction process. A mapping is utilized to transform the internal state variable uncertainties in the form of the state covariance matrix into the output variables, so that uncertainty bounds on these output parameters can be provided. The uncertainty of every derived quantity can be estimated by transforming the internal filter state covariance into the output coordinates. This mapping can be made by using the central difference transform, which provides second-order accuracy and does not require the use of any partial derivatives. The transformation is given in Ref. 15.

MEASUREMENT SENSOR MODELING AND PREPROCESSING

The following sections provide details of the various sensor models and data that were acquired for trajectory and atmosphere reconstruction. These data consist of orbit determination solutions for initial conditions, IMU accelerations and rates, MEADS pressure sensors, on-board radar, and the measured landing site. Also, atmospheric models required to produce data outside the range of the MEADS measurements are described. All times are referenced to a $t - t_0$ where $t_0 = 397501174.997338$ s in Spacecraft Clock Time (SCLK).

Inertial Measurement Unit Data

Data from the onboard IMU, consisting of ΔVs and $\Delta\theta$s were acquired at a rate of 200 Hz. These velocity and attitude increments were converted into acceleration and angular rate by dividing by the time step for each measurement. A Tustin bilinear filter was used to smooth the data for use in the reconstruction of aerodynamics. Unfiltered data was integrated in the Kalman filter equations of motion. The filtered and unfiltered accelerations are shown in Fig. 4 and the angular rate data are shown in Fig. 5. Note that considerable noise due to structural vibrations occur during the bank reversal maneuvers where the RCS jets are active. The bias, scale factor, misalignment, noise, and quantization for both the gyroscopes and the accelerometers are combined together as consider parameters for the weighting in the reconstruction algorithm. Further information on the IMU specifications can be found in Ref. 16.

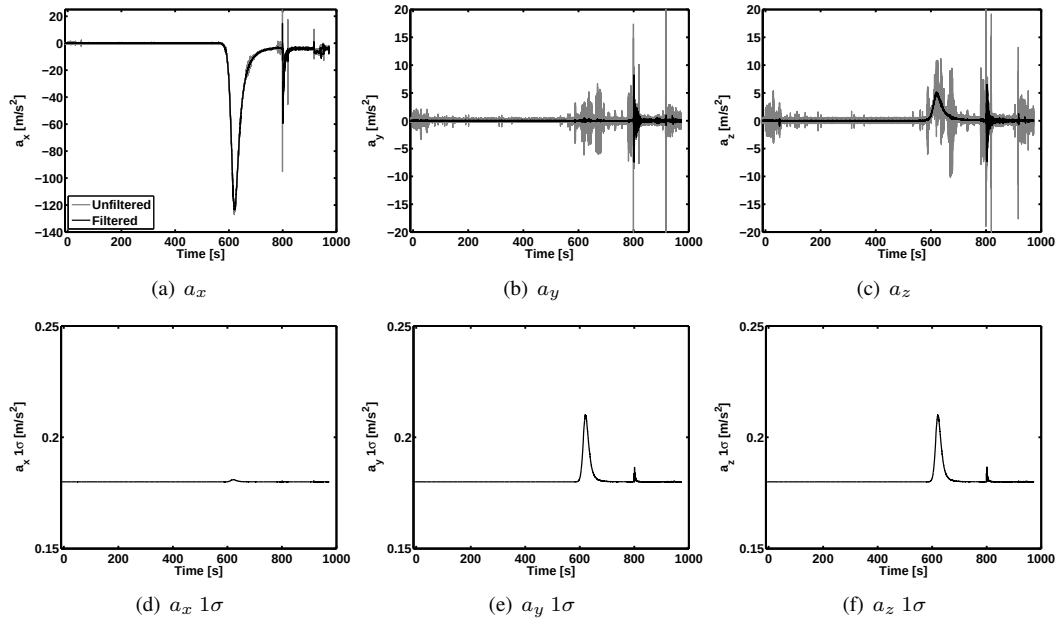

(a) a_x (b) a_y (c) a_z

(d) a_x 1σ (e) a_y 1σ (f) a_z 1σ

Figure 4. IMU Accelerations

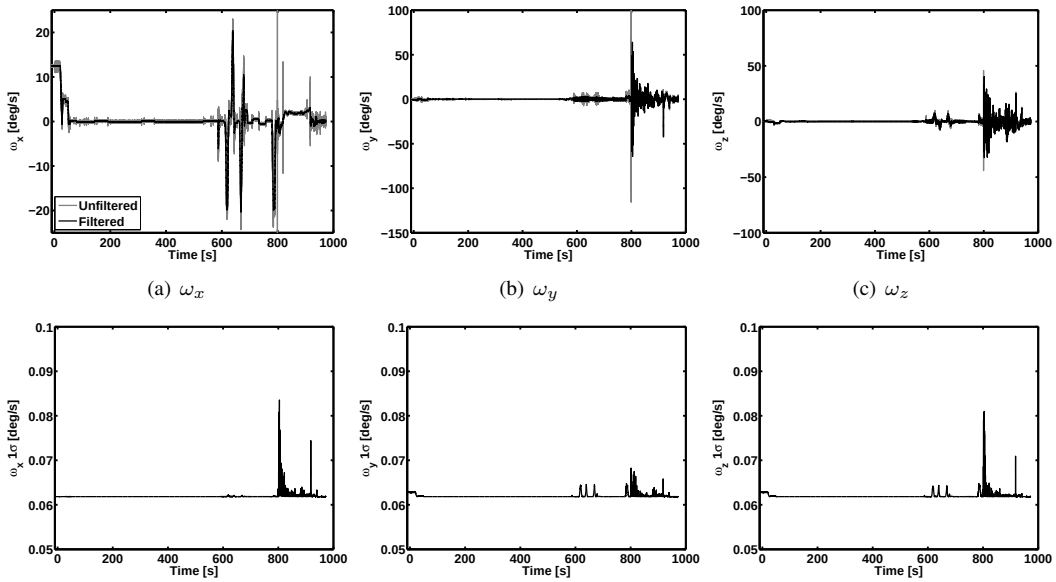

(a) ω_x (b) ω_y (c) ω_z

(d) ω_x 1σ (e) ω_y 1σ (f) ω_z 1σ

Figure 5. IMU Angular Rates

The initial conditions for the integration are based on the orbit determination (OD) number 230, which provides the position and velocity of the vehicle in the Earth Mean Equator of J2000 (EMEJ2000) coordinate system at a time of approximately 550 seconds prior to entry interface (t_0-10 s).[17] The attitude initialization was based on the on-board navigation filter that performed a star tracker alignment prior to cruise stage separation. This attitude solution was then propagated to the same initial time as the OD230 solution by numerical integration.

Mars Entry Atmospheric Data System

A CFD-based table lookup model was developed for analysis of the MSL air data system. This CFD database is based on supersonic and hypersonic regime pressure distributions from thin–layer Navier–Stokes solutions generated using the Langley Aerothermal Upwind Relaxation Algorithm (LAURA).[18,19] The relaxation of vibrational temperature of the CO_2 molecule is simulated using the Camac[20] model. Forebody solutions were obtained using a 7 block singularity-free grid.

The supplied CFD database was converted from absolute pressure to pressure coefficient in order to allow the pressure distribution to scale with different trajectories and to enable estimation of freestream atmospheric properties such as the static pressure. The data was re–interpolated from the 7 block grid to a single-zone grid of clock and cone angles. This alteration simplifies the interpolation of surface conditions without complications of search routines required to handle multiple zones. Note that each CFD grid point consists of a full surface pressure distribution solution, with 37 clock angles in uniform 5 deg increments and 61 cone angles with non-uniform increments. These grid points can be interpolated as needed to provide estimates of the pressure distribution at any point on the aeroshell.

Note that the pressure model utilized for atmospheric state estimation is based entirely on these tabulated CFD solutions. The CFD modeling approach was validated in air in wind tunnel experiments at Mach numbers of 2.5, 3.5, 4.5, and 10. The residuals between computed and measured pressure distribution were within the measurement accuracy of the wind tunnel, which provides confidence in the modeling approach for MEADS.

An uncertainty model of the CFD pressure distribution was developed to consider various error sources, including basic wind tunnel to CFD differences, errors inherent to the wind tunnel data, deformation, OML change, grid refinement, ablation, protuberances, and port location uncertainties. Pressure measurement system error models consist of detailed transducer characterizations from thermal vacuum chamber calibrations, thermocouple measurement errors such that an inaccurate temperature is used in the calibration database, system noise and quantization, time tag errors and sampling delays, pressure path leaks, pneumatic lag, and thermal transpiration.[11] These error models are combined together to produce measurement uncertainty inputs required by the reconstruction algorithm.

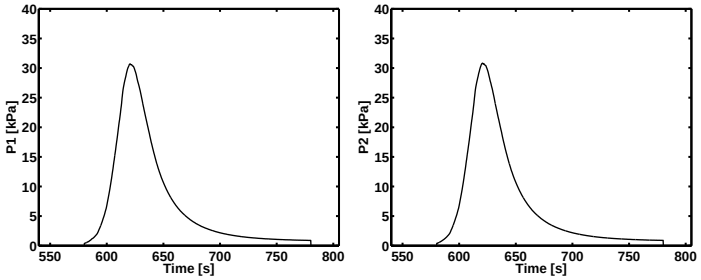

(a) Port 1 (b) Port 2

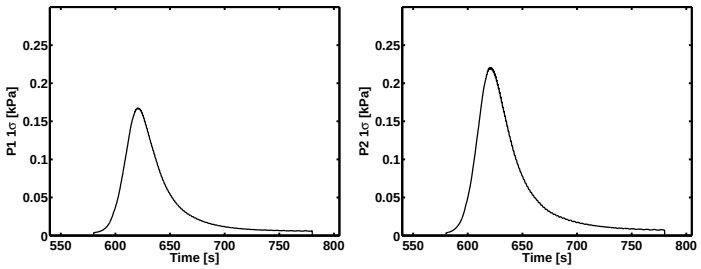

(c) Port 1 1σ (d) Port 2 1σ

Figure 6. MEADS Ports 1 and 2

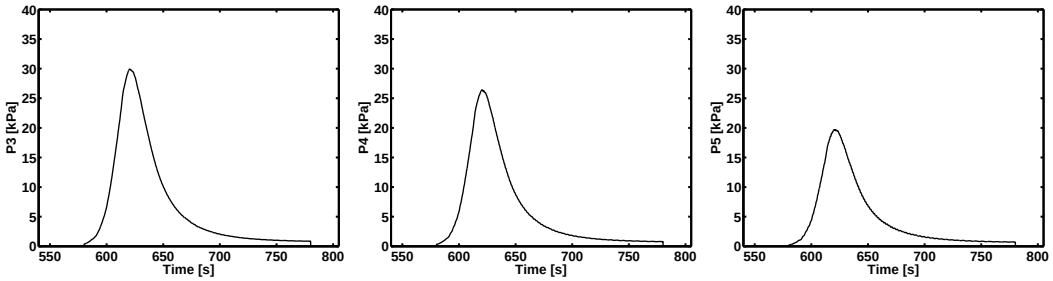

(a) Port 3 (b) Port 4 (c) Port 5

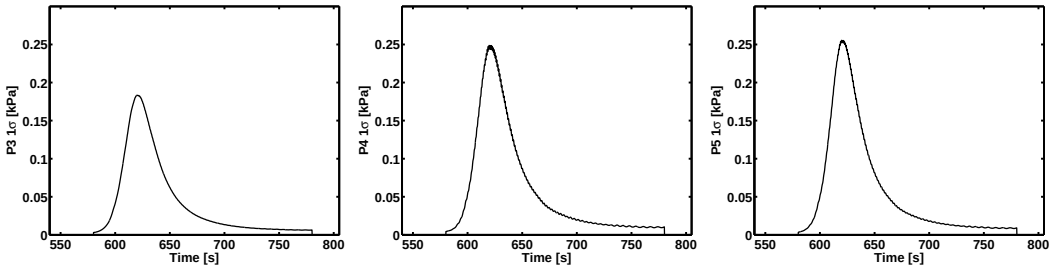

(d) Port 3 1σ (e) Port 4 1σ (f) Port 5 1σ

Figure 7. MEADS Ports 3, 4, and 5

The MEADS pressure measurement data were acquired at an 8 Hz sample rate during EDL. For EDL reconstruction, the data were first converted into engineering units, after which an in-flight zero was applied to correct for transducer thermal drift. Subsequently, outlying data points due to the entry ballast mass ejections were edited out and filled in with a first-order polynomial fit, and a 1 Hz optimal Fourier filter was applied to smooth the data. The pressures were then interpolated to the Port 4 time tag in order to generate pressure samples at a common 8 Hz rate. The resulting pressures are shown in Figures 6–8. These figures illustrate that the sensor readings during EDL are reasonable, and that all transducers are functional. Data quality during EDL was good for the majority of the trajectory. Some noise was introduced during pyro events associated with mass ejections during the reorientation to zero angle of attack in preparation for parachute deployment. Vibrations induced by the parachute mortar fire event were large, which further reduced the

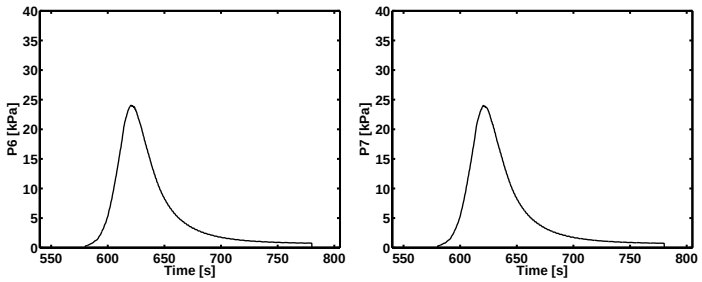

(a) Port 6 (b) Port 7

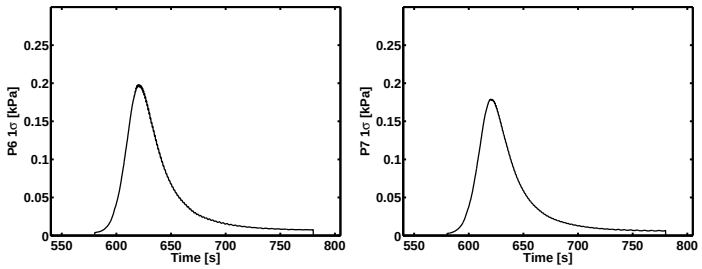

(c) Port 6 1σ (d) Port 7 1σ

Figure 8. MEADS Ports 6 and 7

MEADS data quality. This vibrational noise, coupled with the rapid decrease in dynamic pressure following parachute deployment, limited the last valid MEADS measurement to the instant prior to parachute mortar fire. Other aspects of MEDLI hardware performance during EDL are described in Ref. 21.

Systematic errors are estimated in the MEADS measurements by a batch least-squares regression of post-fit residuals using a second-order error model, consisting of bias, scale factor, and nonlinearity errors. These error estimates are updated through a global iteration process of the Kalman filter.

Terrain Descent Sensor Data

After the MSL heat shield is jettisoned, the Terrain Descent Sensor (TDS) is used to acquire ground range position and relative velocity measurements used by the MSL Navigation Filter.[16] The system consists of six pencil beam antennas located underneath the Curiosity Rover. The TDS system provides slant-range position measurements along the line of sight of the antenna at a rate of 20 Hz. Each frame of data corresponds to a single antenna measurement such that measurements from all six antennas are received individually by the Navigation Filter. In order to match the measurement to the corresponding antenna, a beam identification number is provided to the Navigation Filter along with each measurement.

The TDS model used by NewSTEP relies on a digital elevation model (DEM) implemented. Multiple DEM layers are available for use, each having different levels of resolution. At higher altitudes, the coarser resolution DEMs are used because vehicle oscillations under chutes can cause the antenna beams to swing outside of the range of the higher resolution DEMs. As the vehicle approaches the planet surface, the finer resolution DEMs can be used to provide a higher fidelity TDS measurement. Given the position and orientation vector of the current beam in the Mars-fixed reference frame, the model calls the appropriate resolution DEM to generate a slant-range measurement of the beam intercept location.

The TDS uncertainty model includes noise, bias, scale factor, and misalignment uncertainties that are combined together for a total instrument accuracy. In addition, a 3σ uncertainty of 100 m in the DEM model was assumed. The TDS data and uncertainties for beams 1-3 are shown in Fig. 9 and the same data for beams 4-6 are shown in Fig. 10.

Atmosphere Model

Atmospheric models along the MSL EDL trajectory were generated from preflight mesoscale models, tuned to match surface pressure measurements of 695 Pa from Curiosity, which were obtained after landing. The modeled atmosphere is an average of two such mesoscale models, namely the the Mars Regional Atmospheric Modeling System (MRAMS) and Mars Mesoscale Model 5 (MMM5).[22] These models provide data up to 50 km altitude, which can be extrapolated to higher altitudes as needed. This combined model was queried along the trajectory at a rate of 8 Hz to generate pressure, density, and temperature profiles. These

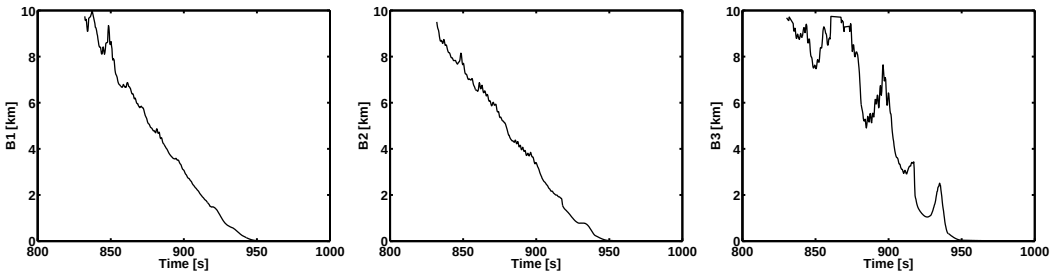

(a) Beam 1 (b) Beam 2 (c) Beam 3

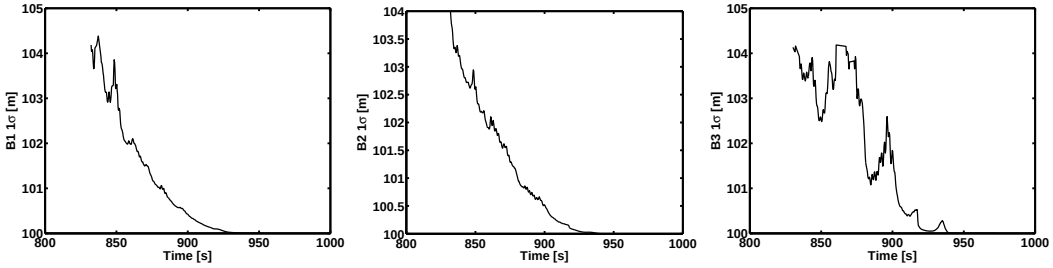

(d) Beam 1 1σ (e) Beam 2 1σ (f) Beam 3 1σ

Figure 9. TDS Beams 1, 2, and 3

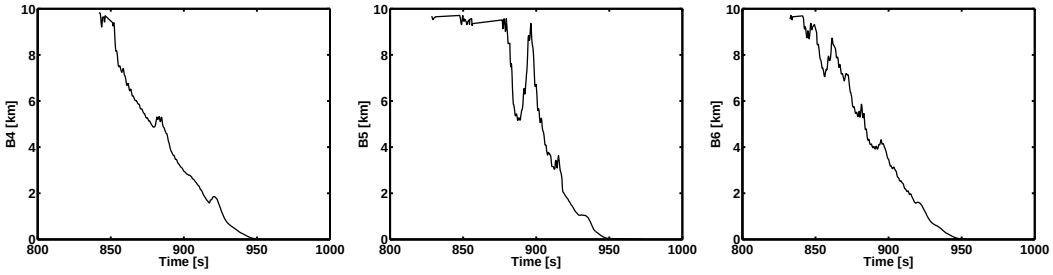

(a) Beam 4 (b) Beam 5 (c) Beam 6

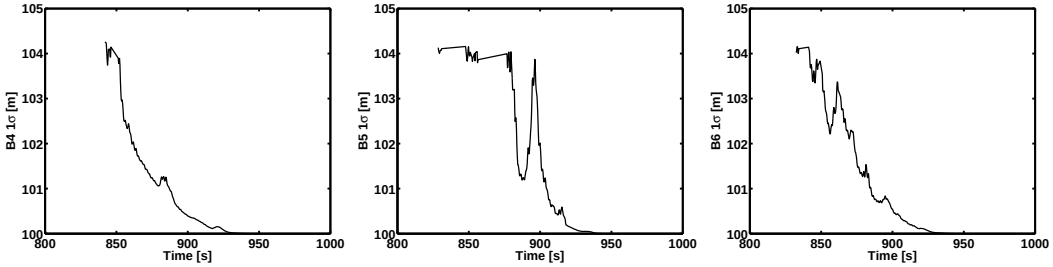

(d) Beam 4 1σ (e) Beam 5 1σ (f) Beam 6 1σ

Figure 10. TDS Beams 4, 5, and 6

models produce estimates of the uncertainty in density, but do not do so for pressure, temperature, or winds. For the filter weighting, it is assumed that the pressure uncertainty is the same percentage as the density uncertainty. Temperature is not used as an independent observation since the filtering approach internally makes use of the equation of state. Winds are assumed to be zero mean along the trajectory with 1σ uncertainties of 10 m/s in north and east directions and 2.5 m/s in the down direction.

Landing Site

MSL's landing site location was determined based on MARDI descent images and a HiRISE-derived map of the surface. The landing site location is processed as a position measurement in the Kalman filter reconstruction at the time of touchdown. The uncertainty in the measurement is assumed to be 50 m in a 3σ sense. The measured landing position is given in Table 3.

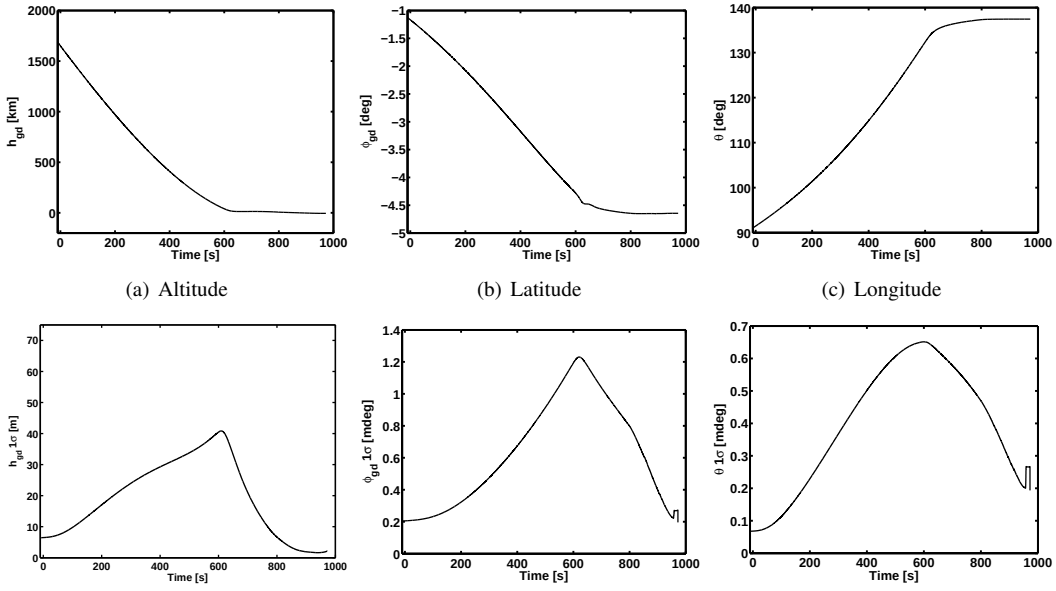

(a) Altitude (b) Latitude (c) Longitude

(d) Altitude 1σ (e) Latitude 5 1σ (f) Longitude 6 1σ

Figure 11. Position Estimates

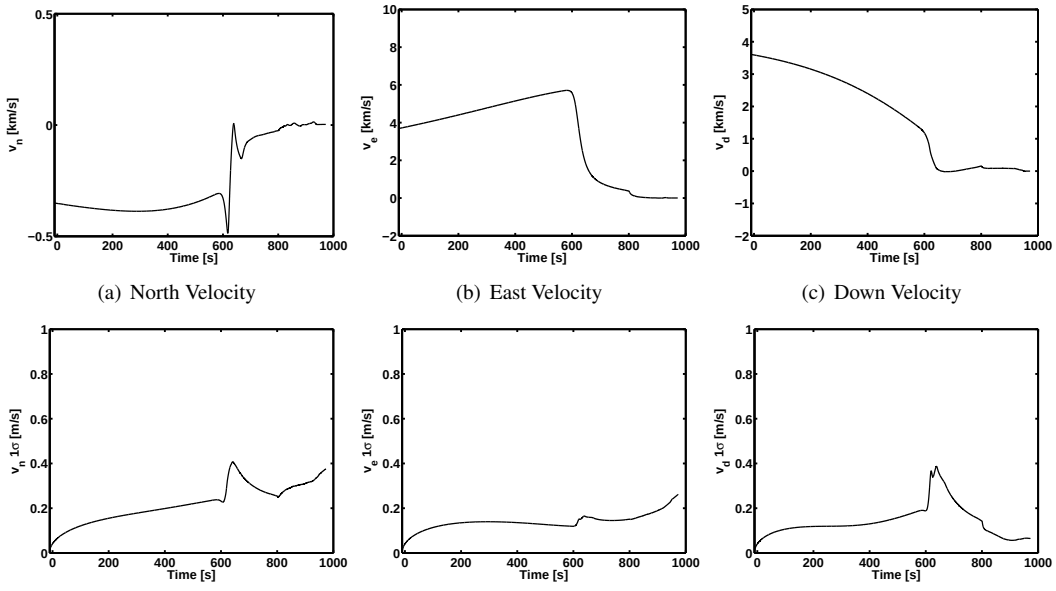

(a) North Velocity (b) East Velocity (c) Down Velocity

(d) North Velocity 1σ (e) East Velocity 5 1σ (f) Down Velocity 6 1σ

Figure 12. Velocity Estimates

The results of the trajectory reconstruction process are described in this section. Fig. 11 shows the altitude, latitude, and longitude results along with their associated 1σ uncertainties. Fig. 12 shows the north/east/down components of the planet-relative velocity and 1σ uncertainties. Similarly, Fig. 13 shows the time history of the yaw/pitch/roll attitude estimates.

Atmospheric-relative quantities are shown in Figs. 14 and 15. Fig. 14 shows the wind-relative angle of attack and sideslip reconstructions compared with the planet-relative (no wind) angles. The time scale is focused on the range from atmospheric interface to parachute deployment. Here, the wind-relative angles are shown in grey and the planet-relative angles are shown in black. The two angles match fairly well in the regime of hypersonic flight, which is expected since the wind magnitudes are relatively small compared

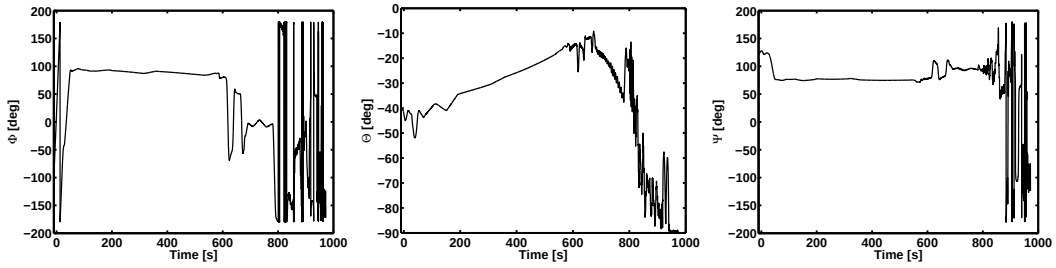

(a) Roll (b) Pitch (c) Yaw

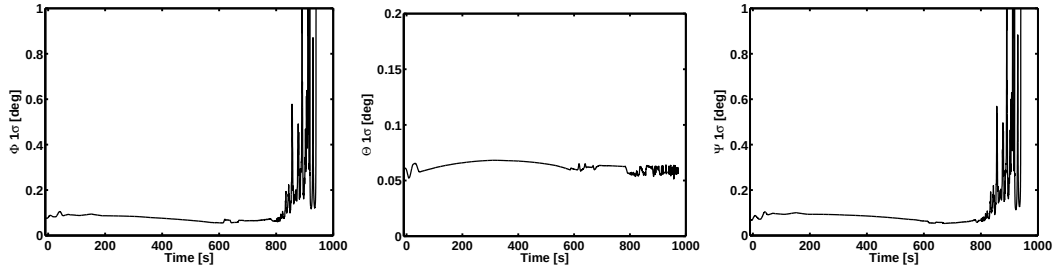

(d) Roll 1σ (e) Pitch 5 1σ (f) Yaw 6 1σ

Figure 13. Attitude Estimates

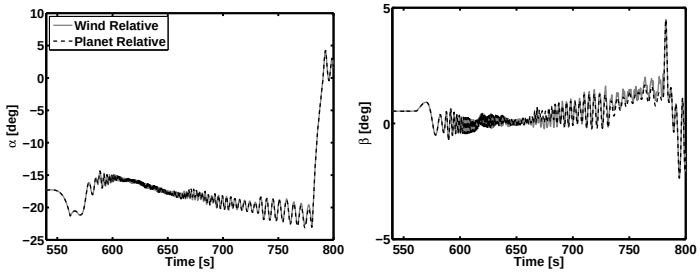

(a) Angle of Attack (b) Angle of Sideslip

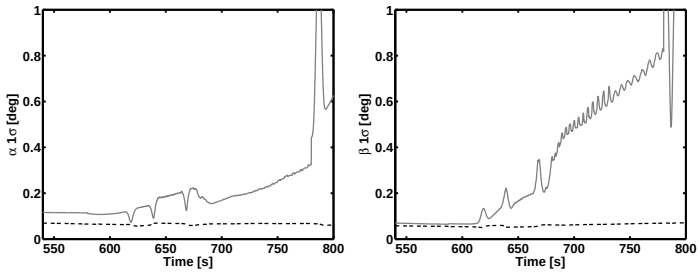

(c) Angle of Attack 1σ (d) Angle of Sideslip 1σ

Figure 14. Angles of Attack and Sideslip Estimates

with the total vehicle velocity. As the vehicle decelerates, the angles start to become more sensitive to winds. The observability of wind-relative angles is enabled by the MEADS pressure measurements. There is an apparent wind event near t=670 s, as can be seen from the difference between the wind-relative and planet-relative angles of attack. There is supporting evidence of such an event from the vehicle response to guidance commands, which is discussed in more detail in Ref. 23. Wind profiles reconstructed from these data are shown later in this section.

The estimates of Mach number and dynamic pressure are shown in Fig. 15. These time histories are also enabled by the MEADS measurements, which provide estimates of the freestream atmosphere, that when combined with velocity can be used to compute estimates of Mach number and dynamic pressure. The improvement in uncertainties due to the MEADS measurements in the range of 590 to 780 s can clearly be

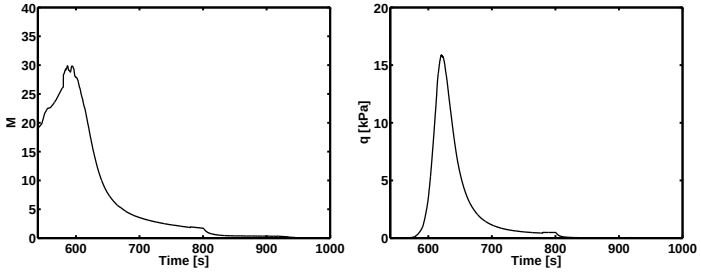

(a) Mach Number (b) Dynamic Pressure

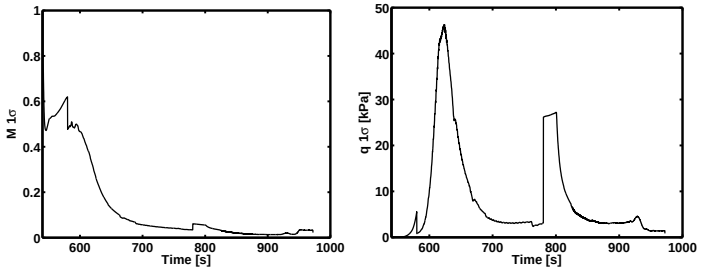

(c) Mach Number 1σ (d) Dynamic Pressure 1σ

Figure 15. Mach Number and Dynamic Pressure

seen in these figures.

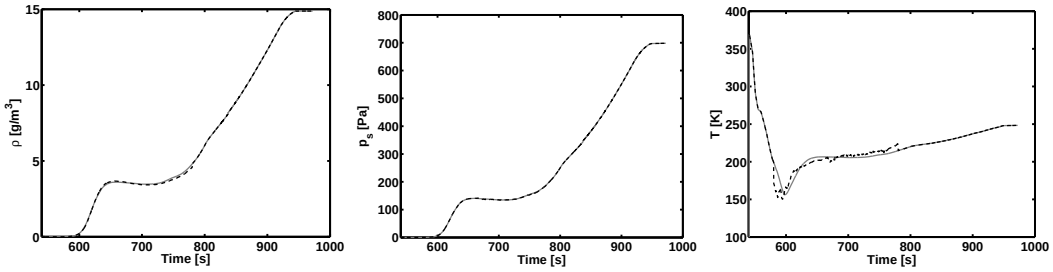

(a) Density (b) Pressure (c) Temperature

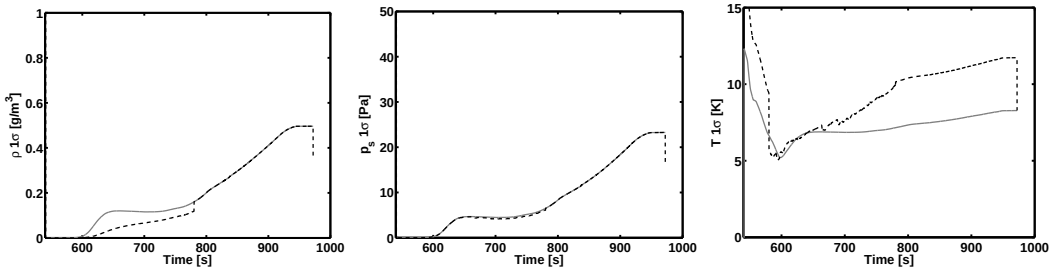

(d) Density 1σ (e) Pressure 1σ (f) Temperature 1σ

Figure 16. Atmosphere Estimates

The atmospheric outputs of the reconstruction filter are shown in Figs. 16. Here, the filter outputs are shown in black and the mesoscale model data is shown in grey for comparison. While the MEADS measurements are being processed, the filter is able to identify the atmospheric conditions. The filter tracks the mesoscale model inputs when the MEADS measurements are not available.

Estimates of atmospheric winds in the north/east/down frame relative to the planet surface are shown in Fig. 17. These result suggest that a north wind component (which is essentially a cross wind) could be the cause of the guidance disturbance near t=670 s.[23] These results also suggest a tail wind present as the vehicle neared the chute deployment condition.

The reconstructed axial and normal aerodynamic force coefficients are shown in Fig. 18. These plots

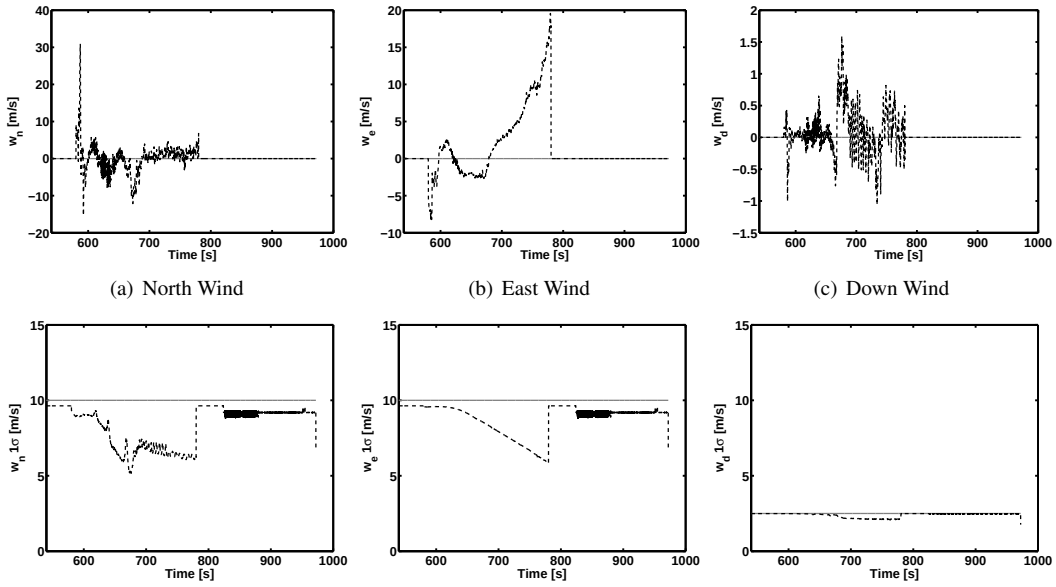

(a) North Wind (b) East Wind (c) Down Wind

(d) North Wind 1σ (e) East Wind 1σ (f) Down Wind 1σ

Figure 17. Wind Estimates

compare the reconstructed aerodynamics in the black curve to the nominal aerodatabase queried along the reconstructed trajectory in grey. These results indicate a roughly 2% higher than nominal axial force, which is in agreement with the results from the semi-independent reconstructions presented in Ref. 2. Note that the aerodatabase uncertainties shown include the actual database uncertainties as well as uncertainties in the reconstructed trajectory on which the database is queried. The aerodynamic moment reconstruction is shown in Fig. 19. These moments are about the vehicle center of mass. A complete reconciliation of the aerodynamic model is beyond the scope of this paper; a more detailed description of the aerodynamic reconstruction and model reconciliation can be found in Ref. 24.

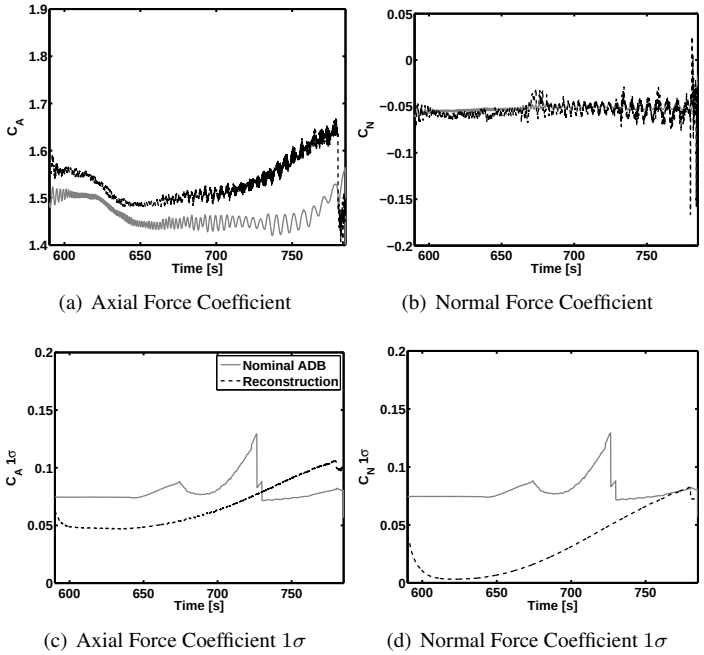

(a) Axial Force Coefficient (b) Normal Force Coefficient

(c) Axial Force Coefficient 1σ (d) Normal Force Coefficient 1σ

Figure 18. Aerodynamic Force Reconstruction

Residuals between the reconstructed trajectory and the MEADS measurement data are shown in Fig. 20. The $\pm 3\sigma$ thresholds based on the residual covariance are also shown. These results indicate that the residuals

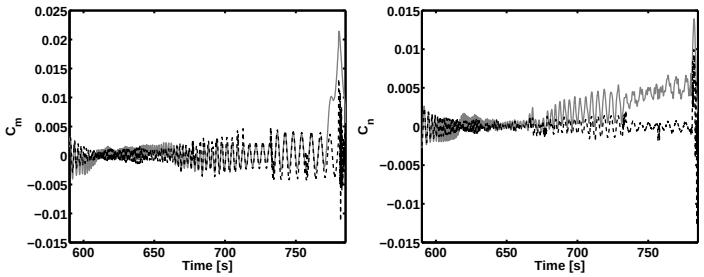

(a) Pitch Moment Coefficient (b) Yaw Moment Coefficient

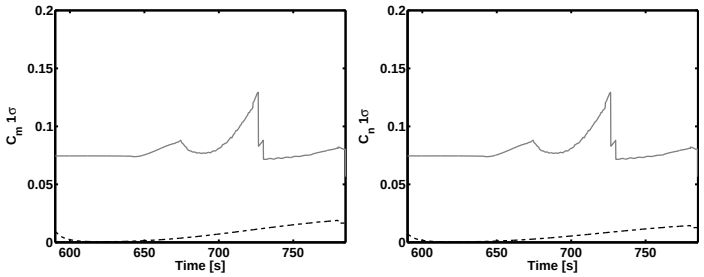

(c) Pitch Moment Coefficient 1σ (d) Yaw Moment Coefficient 1σ

Figure 19. Aerodynamic Moment Reconstruction

Table 1. MEADS Systematic Error Estimates

Port	Bias (Pa)	Scale Factor	Nonlinearity (1/Pa)
1	-3.19	1.54E-03	-1.83E-08
2	-2.39	1.23E-03	-1.29E-08
3	0.06	2.35E-04	-1.54E-09
4	2.18	-1.10E-03	1.48E-08
5	4.60	-3.95E-03	8.68E-08
6	3.95	-1.78E-03	2.00E-08
7	0.42	-8.42E-04	2.45E-09

fall within the filter uncertainty predictions and thus the filter is consistent. A summary of the systematic error estimates in the MEADS data is shown in Table 1. The TDS residuals are shown in Fig. 21, which also indicate consistent filter performance.

The inertial trajectory components are compared to measurement data in Tables 2 and 3. Table 2 shows a comparison of the measured initial condition from OD 230 compared to the reconstructed initial condition from the Kalman filter output. The measured and reconstructed landing site location is compared in Table 3. In each case, the 1σ uncertainties shown in both the measured and reconstructed values.

CONCLUSIONS

This paper describes a Kalman Filtering approach that has been implemented for Mars Science Laboratory entry, descent, and landing trajectory and atmosphere reconstruction. The methods makes use of the total available data to reconstruct the trajectory and atmosphere from cruise stage separation to landing. This paper describes the algorithm formulation, uncertainty models, and details of the processing of the data to produce estimates of the trajectory, atmosphere, winds, and aerodynamics. In addition, uncertainties on all reconstructed data are produced by the filter.

The data sources considered in the Kalman filtering approach include the inertial measurement unit accelerations and angular rates, the terrain descent sensor, the measured landing site, orbit determination solutions for the initial conditions, and a new set of instrumentation for planetary entry reconstruction consisting of forebody pressure sensors, known as the Mars Entry Atmospheric Data System. These pressure measure-

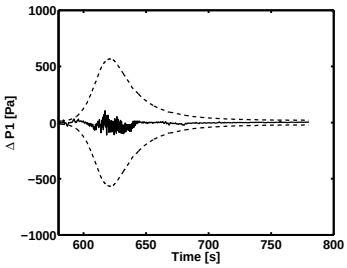

(a) Port 1 Residual

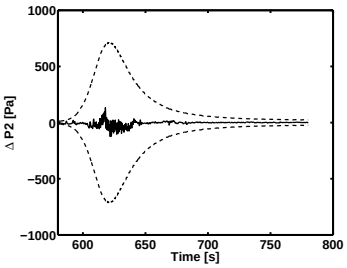

(b) Port 2 Residual

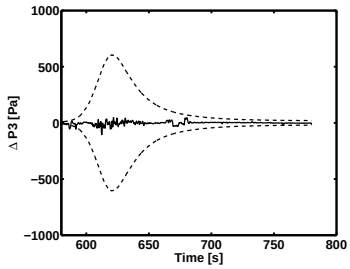

(c) Port 3 Residual

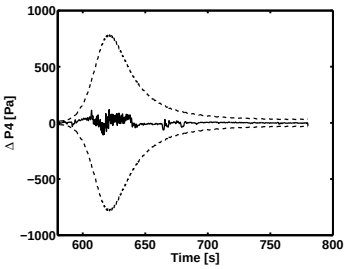

(d) Port 4 Residual

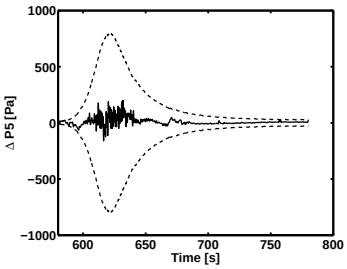

(e) Port 5 Residual

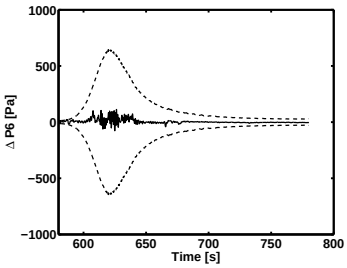

(f) Port 6 Residual

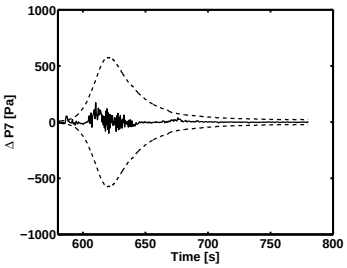

(g) Port 7 Residual

Figure 20. MEADS Residuals

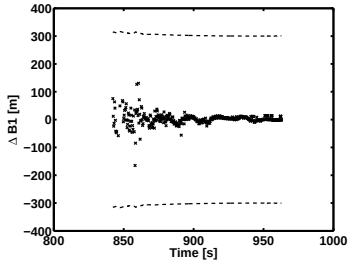

(a) Beam 1 Residual

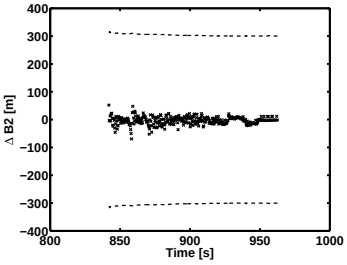

(b) Beam 2 Residual

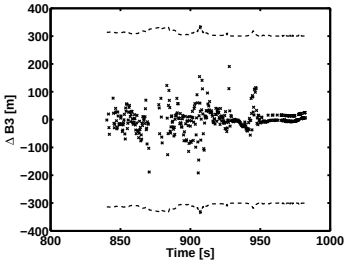

(c) Beam 3 Residual

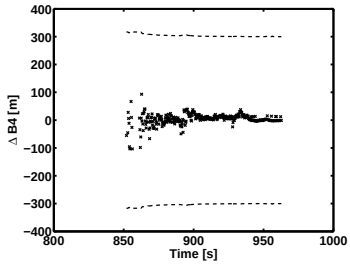

(d) Beam 4 Residual

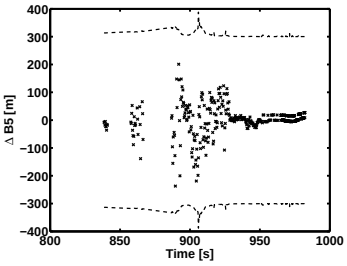

(e) Beam 5 Residual

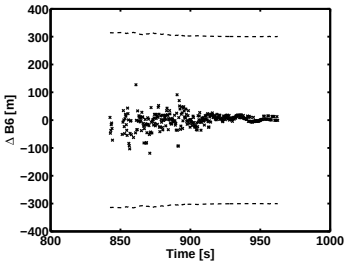

(f) Beam 6 Residual

Figure 21. TDS Residuals

Table 2. Initial Conditions

State	OD/Nav State		Filter Estimates	
	State	1σ Uncertainty	State	1σ Uncertainty
r, m	5082657.04	6.46	5082655.62	6.44
ϕ, deg	-1.11749	2.04e-04	-1.11753	2.04E-04
θ, deg	91.05201	6.78e-05	91.05201	6.76E-4
u, m/s	-349.691	0.012	-349.693	0.012
v, m/s	4047.656	0.008	4047.658	0.008
w, m/s	3608.537	0.009	3608.538	0.009
Φ, deg	-103.744	0.033	-103.743	0.079
Θ, deg	-42.090	0.033	-42.096	0.059
Ψ, deg	121.742	0.033	121.726	0.071

Table 3. Landing Site Location

State	OD/Nav State		Filter Estimates	
	State	1σ Uncertainty	State	1σ Uncertainty
r, m	3391133.3	16.7	3391157.7	2.7
ϕ, deg	-4.5895	2.81e-04	-4.5898	1.96e-04
θ, deg	137.4417	2.81e-04	137.4406	1.94e-04

ments are unique for planetary entry, descent, and landing reconstruction as they enable a reconstruction of the freestream atmospheric conditions without any prior assumptions being made on the vehicle aerodynamics. Moreover, the processing of the MEADS measurements in the Kalman filter approach enables the identification of atmospheric winds, which has not been accomplished in past planetary entry reconstructions. This separation of atmosphere and aerodynamics allows for aerodynamic model reconciliation and uncertainty quantification, which directly impacts future missions.

Future reconstruction work will be focused on incorporating the terrain descent sensor Doppler velocity measurements and improved gravity models for Gale crater into the Kalman filter approach.

ACKNOWLEDGEMENTS

The authors are grateful to Chris Kuhl for extraction of the binary MEADS pressure and temperature data, Alicia Dwyer Cianciolo for providing the mesoscale model data, John Van Norman for providing the MSL CFD pressure model and associated uncertainty model, and to Fred Serricchio and David Way for assistance with the IMU data.

REFERENCES

[1] Munk, M. M., Little, A., Kuhl, C., Bose, D., and Santos, J., "The Mars Science Laboratory (MSL) Entry, Descent, and Landing Instrumentation (MEDLI) Hardware," AAS Paper 13-310, February 2013.

[2] Karlgaard, C. D., Kutty, P., Shidner, J., Schoenenberger, M., and Munk, M. M., "Mars Entry Atmospheric Data System Trajectory Reconstruction Algorithms and Flight Results," AIAA Paper 2013-0028, January 2013.

[3] Bose, D., White, T., Santos, J. A., Mahzari, M., and Edquist, K., "A Reconstruction of Aerothermal Environment and Thermal Protection System Response of the Mars Science Laboratory Entry Vehicle," AAS Paper 13-311, February 2013.

[4] Abilleira, F. and Shidner, J., "Entry, Descent, and Landing Communications for the 2011 Mars Science Laboratory," Paper IN1-4, 23rd International Symposium on Space Flight Dynamics, Pasadena, CA, October 2012.

[5] Steltzner, A. D., *et al*, "Mars Science Laboratory Entry, Descent, and Landing System Overview," AAS Paper 13-236, February 2013.

[6] Wagner, W. E., "Re-Entry Filtering, Prediction, and Smoothing," *Journal of Spacecraft and Rockets*, Vol. 3, No. 9, 1966, pp. 1321–1327.

[7] Wagner, W. E. and Serold, A. C., "Formulation on Statistical Trajectory Estimation Programs," NASA CR-1482, January 1970.

[8] Karlgaard, C. D., Tartabini, P. V., Blanchard, R. C., Kirsch, M., and Toniolo, M. D., "Hyper–X Post–Flight Trajectory Reconstruction," *Journal of Spacecraft and Rockets*, Vol. 43, No. 1, 2006, pp. 105–115.

[9] Karlgaard, C. D., Tartabini, P. V., Martin, J. G., Blanchard, R. C., Kirsch, M., Toniolo, M. D., and Thornblom, M. N., "Statistical Estimation Methods for Trajectory Reconstruction: Application to Hyper-X," NASA TM-2009-215792, August 2009.

[10] Karlgaard, C. D., Beck, R. E., Derry, S. D., Brandon, J. M., Starr, B. R., Tartabini, P. V., and Olds, A. D., "Ares I-X Trajectory Reconstruction: Methodology and Results," *Journal of Spacecraft and Rockets*, accepted.

[11] Karlgaard, C. D., Beck, R. E., O'Keefe, S. A., Siemers, P. M., White, B. A., Engelund, W. C., and Munk, M. M., "Mars Entry Atmospheric Data System Modeling and Algorithm Development," AIAA Paper 2009-3916, June 2009.

[12] Fraser, D. C. and Potter, J. E., "The Optimum Linear Smoother as a Combination of Two Optimum Linear Filters," *IEEE Transactions on Automatic Control*, Vol. 14, No. 8, 1969, pp. 387–390.

[13] Crassidis, J. L. and Junkins, J. L., *Optimal Estimation of Dynamic Systems*, Chapman & Hall/CRC, Boca Raton, FL, 2004.

[14] Kelly, G. M., Findlay, J. T., and Compton, H. R., "Shuttle Subsonic Horizontal Wind Estimation," *Journal of Spacecraft and Rockets,* Vol. 20, No. 4, 1983, pp. 390–397.

[15] Nørgaard, M., Poulsen, N. K., and Ravn, O., "New Developments in State Estimation for Nonlinear Systems," *Automatica*, Vol. 36, No. 11, 2000, pp. 1627-1638.

[16] Serricchio, F., San Martin, A. M., and Wong, E. C., "The MSL Navigation Filter," AAS Paper 13-418, February 2013.

[17] Martin-Mur, T. J., Kruizinga, G., and Wong, M., "Mars Science Laboratory Interplanetary Navigation Performance," AAS Paper 13-232, February 2013.

[18] Schoenenberger, M., Dyakonov, A., Buning, P., Scallion, W., and Van Norman, J., "Aerodynamic Challenges for the Mars Science Laboratory Entry, Descent and Landing," AIAA Paper 2009-3914, June 2009.

[19] Dyakonov, A., Schoenenberger, M., and Van Norman, J., "Hypersonic and Supersonic Static Aerodynamics of Mars Science Laboratory Entry Vehicle," AIAA Paper 2012-2999, June 2012.

[20] Camac, M., "CO2 Relaxation Process in Shock Waves," in *Fundamental Phenomena in Hypersonic Flow*, Hall, J. G. (Ed.), Cornell University Press, Ithaca, New York, 1966.

[21] Little, A., Munk, M., Schoenenberger, M., Kuhl, C., Antill, C., Verhappen, R., Karlgaard, C., Kutty, P., Bose, D., and White, T., "The Mars Science Laboratory (MSL) Entry, Descent and Landing Instrumentation (MEDLI): Hardware Performance and Data Reconstruction," AAS Paper 13-078, February 2013.

[22] Vasavada, A. R., Chen, A., Barnes, J. R., Burkhart, P. D., Cantor, B. A., Dwyer-Cianciolo, A. M., Fergason, R. L., Hinson, D. P., Justh, H. L., Kass, D. M., Lewis, S. R., Mischna, M. A., Murphy, J. R., Rafkin, S. C. R., Tyler, D., and Withers, P. G., "Assessment of Environments for Mars Science Laboratory Entry, Descent, and Surface Operations," *Space Science Reviews*, Vol. 170, 2012, pp. 793–835.

[23] Mendeck, G. and McGrew, L., "Post-Flight EDL Entry Guidance Performance of the 2011 Mars Science Laboratory Mission," AAS Paper 13-419, February 2013.

[24] Schoenenberger, M., Van Norman, J., Dyakonov, A., Karlgaard, C. D., Way, D., and Kutty, P., "Preliminary Comparison of Preflight and Reconstructed Aerodynamics of the Mars Science Laboratory Entry Vehicle," AAS Paper 13-306, February 2013.